ADVANCED QUANTUM TECHNOLOGIES
www.advquantumtech.com

Engineering Epitaxial Interfaces for Topological Insulator — Superconductor Hybrid Devices with Al Electrodes

Abdur Rehman Jalil, Tobias W. Schmitt, Philipp Rüßmann, Xian-Kui Wei, Benedikt Frohn, Michael Schleenvoigt, Wilhelm Wittl, Xiao Hou, Anne Schmidt, Kaycee Underwood, Gustav Bihlmayer, Martina Luysberg, Joachim Mayer, Stefan Blügel, Detlev Grützmacher, and Peter Schüffelgen**

Proximity-induced superconductivity in hybrid devices of topological insulators and superconductors offers a promising platform for the pursuit of elusive topological superconductivity and its anticipated applications, such as fault-tolerant quantum computing. To study and harness such hybrid devices, a key challenge is the realization of highly functional material interfaces with a suitable superconductor featuring 2*e*-periodic parity-conserving transport to ensure a superconducting hard-gap free of unpaired electrons, which is important for Majorana physics. A superconductor well-known for this characteristic is Al, however, its direct integration into devices based on tetradymite topological insulators has so far been found to yield non-transparent interfaces. By focusing on Bi_2Te_3-Al heterostructures, this study identifies detrimental interdiffusion processes at the interface through atomically resolved structural and chemical analysis, and showcases their mitigation by leveraging different interlayers – namely Nb, Ti, Pd, and Pt – between Bi_2Te_3 and Al. Through structural transformation of the interlayer materials (X) into their respective tellurides (XTe_2) atomically-sharp epitaxial interfaces are engineered and further characterized in low-temperature transport experiments on Al-X-Bi_2Te_3-X-Al Josephson junctions and in complementary density functional theory calculations. By demonstrating functional interfaces between Bi_2Te_3 and Al, this work provides key insights and paves the way for the next generation of sophisticated topological devices.

1. Introduction

The discovery of topological superconductivity has ushered in a new era in condensed matter physics, with potential applications in quantum computing and beyond.[1] Topological superconductors (TSCs) are distinguished by their potential to host Majorana zero modes, which are crucial for fault-tolerant topological quantum computing.[2–6] Although naturally occurring TSCs are scarce, they can be artificially engineered by inducing the superconducting proximity effect in topologically protected surface states using a hybrid topological insulator (TI)–superconductor (SC) structure.[7–10] A key element at the heart of these hybrid architectures is a highly functional interface.[10–12] The implementation of such an interface in TI-based heterostructures is, however, challenging.[13] Characteristics such as crystallinity, lattice compatibility and atomic-scale uniformity of a hybrid interface affect the quality of the proximity-induced superconductivity and thus the effective manifestation of the Majorana zero modes.[10,13–15] Conversely, imperfections

A. R. Jalil, T. W. Schmitt, B. Frohn, M. Schleenvoigt, W. Wittl, A. Schmidt, K. Underwood, D. Grützmacher, P. Schüffelgen
Peter Grünberg Institute PGI-9
Forschungszentrum Jülich GmbH
52425 Jülich, Germany
E-mail: a.jalil@fz-juelich.de; p.schueffelgen@fz-juelich.de

The ORCID identification number(s) for the author(s) of this article can be found under https://doi.org/10.1002/qute.202400343

DOI: 10.1002/qute.202400343

A. R. Jalil, T. W. Schmitt, B. Frohn, M. Schleenvoigt, X. Hou, A. Schmidt, S. Blügel, D. Grützmacher, P. Schüffelgen
JARA-FIT (Fundamentals of Future Information Technology)
Jülich-Aachen Research Alliance
Forschungszentrum Jülich and RWTH Aachen University
52425 Jülich, Germany

P. Rüßmann, G. Bihlmayer, S. Blügel
Peter Grünberg Institute PGI-1
Forschungszentrum Jülich GmbH
52425 Jülich, Germany

P. Rüßmann
Institute for Theoretical Physics and Astrophysics
University of Würzburg
97074 Würzburg, Germany

such as defects and lattice-induced strain can lead to the induction of a soft-gap, causing decoherence of Majorana states, which can be detrimental to topological quantum applications.[10,16,17] The exact requirements and associated challenges for achieving a highly functional interface are strongly influenced by the individual characteristics of the TI and SC of choice.[12]

While researchers have explored a variety of SCs for TI-SC hybrid systems, including Nb, Sn, Pb, $NbSe_2$ and $PdTe_2$,[15,18–23] a promising candidate for advanced topological applications is Al due to its ability to enable 2*e*-periodic parity-preserving transport,[24] as exemplified in superconducting quantum circuits.[25,26] Furthermore, for III-V semiconductor hybrids, Al has been shown to be advantageous for the realization of induced superconducting hard gaps.[27,28] Therefore, the implementation of Al as a parent SC could be a decisive step forward for TI-SC hybrid devices. In terms of TI selection, the $Bi_{2-x}Sb_xTe_3$ family offers significant advantages considering the possibility to tune the Fermi level into the bulk gap and the ability to grow reproducibly via molecular beam epitaxy (MBE).[12,29] Nevertheless, these TIs pose significant challenges in attaining atomically clean interfaces, mainly due to their delicate van der Waals (vdW)-based layered structure, susceptibility to point defect formation at room temperature, surface oxidation and aging.[30–32] In addition, the inherent structural incompatibility between trigonal $Bi_{2-x}Sb_xTe_3$ and the majority of s-wave SCs such as Al, which are cubic, as well as diffusion-induced variations in interfacial chemistry, further exacerbate the problem.[30] Given the challenges of surface oxidation and aging, our recently reported UHV-compatible approach provides an ideal platform for investigating TI-SC hybrid devices while ensuring pristine interfaces.[33,34] This platform has already demonstrated highly transparent Nb-$Bi_{2-x}Sb_xTe_3$-Nb Josephson junctions (JJs). However, when substituted with Al, none of the junctions exhibited a Josephson supercurrent; instead, an increase in the junction resistance at low temperatures was observed, indicating the presence of a diffusion-induced suboptimal interface despite fabrication under UHV conditions.[35] Therefore, it is imperative to thoroughly investigate and understand the structural and chemical properties at the interface to effectively tackle the pressing issues related to interdiffusion for future Al-based TI-SC hybrid systems.

To this end, an atomic-scale analysis of a fully in situ prepared $Bi_{2-x}Sb_xTe_3$-Al hybrid structure is performed using scanning transmission electron microscopy (STEM) and is shown in Figure S1, Supporting Information. It reveals an interfacial overlap region that is heavily diffused with Sb, Te and Al atoms, presumably forming an electronic barrier. This diffusion problem is likely exacerbated by Sb, which is a well-known dopant and an effective diffusion agent in the CMOS industry. Sb diffusion not only limits the ability to obtain atomically uniform and epitaxial interfaces, but also complicates the chemical comprehension of the interface. Therefore, it is crucial to simplify the situation by removing Sb from the equation in order to have a better understanding of the interfacial chemistry. Consequently, Bi_2Te_3 is employed to further the study of hybrid interfaces.

This study therefore focuses on an in-depth understanding of the structural, chemical, and electronic properties of hybrid structures and facilitates the engineering of epitaxial interfaces with a focus on Bi_2Te_3-Al devices. The research is supported by realistic DFT modeling and low-temperature measurements of lateral JJs. This comprehensive study of TI-SC hybrid interfaces provides a platform to mitigate some of the key challenges in realizing functional devices, paving the way for the next generation of topological quantum networks.

2. Challenges of Bi_2Te_3-Al Interfaces

To elucidate the challenges with Al as the parent SC, fully *in vacuo* junctions with Bi_2Te_3 as the weak link are fabricated. Details can be found in the "Methods" Section. This approach not only allows the selective growth of TIs in the desired shape and dimensions,[30,31] but also enables the realization of superconducting electrodes without breaking the vacuum, thus preventing the TI surface from oxidation and ensuring pristine TI/SC interfaces.[34,36] **Figure 1**a depicts an optical micrograph of a fabricated chip. Since the entire chip was passivated with Al_2O_3 capping, no surface deformation is observed immediately after the Al deposition, as expected. However, optical studies performed a few days later revealed an aging phenomenon, with the Al layer peeling away from the Bi_2Te_3 surface in some areas while remaining adhered in others. Figure 1b,c depicts magnified optical micrographs of normal and delaminated junctions, respectively. Meanwhile, Figure 1d represents a scanning electron microscope (SEM) image of the indicated location in 1b, along with schematics of an atypical, lateral Al-Bi_2Te_3-Al junction.

The similar flaking pattern is also observed in several planar Bi_2Te_3-Al films, ruling out the possibility that this phenomenon can be triggered by the on-chip stencil mask. Meticulous inspections of various devices and films yielded no clear explanation as to why the peeling of Al from the Bi_2Te_3 surface occurs over time. The only difference seems to be that the heat treatment accelerates the peeling process. Given the absence of a reliable electronic connection, the delaminated devices could not be measured, and subsequently, several normal junctions (without delaminated Al) are selected, and the superconducting transport investigations are performed. Figure 1e shows the temperature-dependent differential resistance (dV/dI) of an Al-Bi_2Te_3-Al junction (black) and the reference Al film on the same chip (red). The continuous drop in (dV/dI) of the junction up to 10 K clearly indicates a semi-metallic character of the weak-link, which is consistent with the bulk-dominated transport in Bi_2Te_3 due to the presence of the Fermi level in the conduction band. Below 10 K, the (dV/dI) of the junction remains relatively constant until a significant increase in the resistance is observed at ≈1.3 K, the superconducting transition temperature (T_c) of Al. Upon further temperature reduction, the junction resistance continues to increase, showing

X.-K. Wei, X. Hou, M. Luysberg, J. Mayer
Ernst Ruska-Centre (ER-C) for Microscopy and Spectroscopy with Electrons
Forschungszentrum Jülich GmbH
52425 Jülich, Germany
J. Mayer
Central Facility for Electron Microscopy (GFE)
RWTH Aachen University
52074 Aachen, Germany

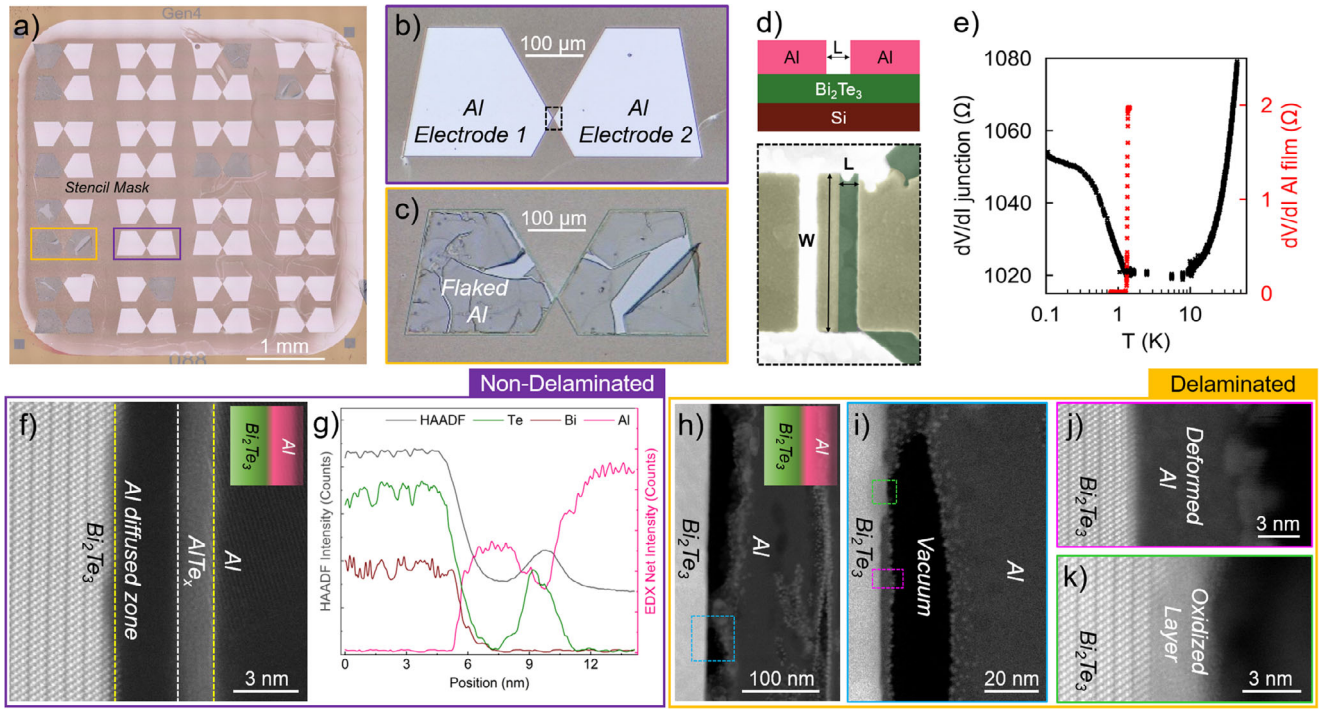

Figure 1. Al as a parent superconductor – challenges: a) Optical micrograph of a fabricated sample using an on-chip stencil mask containing multiple Al-Bi_2Te_3-Al junctions. b) Magnified optical images of the highlighted junctions with normal and c) delaminated Al contacts. d) The schematical representation (side view) along with the scanning electron micrograph of the junction's weak link. e) Temperature-dependent differential resistance (dV/dI) of the junction and the reference Al film, represented by black and red data points, respectively. f) A HAADF image acquired at the cross-section of the non-flaked Al region along with g) the corresponding chemical analysis. h–k) HAADF images at different magnifications, taken at the cross-section of the delaminated Al region showing the remnant amorphous Al and the oxidized Bi_2Te_3 surfaces.

no sign of proximity induced superconductivity, similar to what was observed in the previously discussed $Bi_{2-x}Sb_xTe_3$-Al hybrid junctions.[35] This indicates the presence of a suboptimal (low transparency) Bi_2Te_3/Al interface due to the likely diffusion of Al into the TI epilayer.

Both the normal and delaminated regions have shown signs of poor interface quality, prompting a deeper understanding of the chemical and structural properties at the interfaces. As a result, atomic-scale structural studies are performed at the cross sections of both regions and, as expected, the results are significantly different. A high-angular annular dark-field (HAADF) image obtained at the cross-section of a non-delaminated region, along with the corresponding energy dispersive X-ray (EDX) spectrum, is shown in Figure 1f,g. At the interface, a 4 nm-thick interdiffused region is detected, marked by two yellow dotted lines. Chemical analysis reveals that this region can be further subdivided into two distinct zones. The first zone comprises a 2.5 nm-thick amorphous layer composed predominantly of Al, followed by a 1.5 nm-thick polycrystalline region composed of Al and Te, resulting in the formation of an $AlTe_x$ alloy. $AlTe_x$ is a wide-bandgap semiconductor and its materialization leads to a significant increase in interfacial resistance.[37] This resistance acts as an electronic barrier at the Bi_2Te_3/Al interface, which explains the observed surge in junction resistance below the T_c of Al shown in Figure 1e. Consequently, the formation of $AlTe_x$ at the interface is recognized as the primary reason for the failure to achieve induced superconductivity in Bi_2Te_3 junctions. Above the diffused region, the distinct (220) crystal planes can be clearly observed, indicating the high crystal quality of the Al electrodes.

Figure 1h depicts a large-scale HAADF image acquired at a cross-section of the delaminated surface. The presence of a vacuum (gap) between the Bi_2Te_3 epilayer and Al is evident. The delaminated Al appears to be extremely deformed, as well as having multiple disorienting layers on top of each other. Figure 1i–k presents several magnified images of the highlighted regions to provide a comprehensive view. Figure 1i shows that Al delamination leaves two clearly distinguishable surfaces. In some cases, the delamination leaves a residual amorphous Al layer (Figure 1j); while in other areas, the Al peels off precisely at the interface (Figure 1k), exposing the Bi_2Te_3 surface to oxidation and aging.

In summary, the Bi_2Te_3/Al interfaces present two main challenges that need to be addressed. First, the Al exhibits poor adhesion to the Bi_2Te_3 epilayer; therefore, the interface quality between the epilayer and Al must to be improved. Second, by forming $AlTe_x$, Te prevents Al delamination at the interface. The improved adhesion provided by $AlTe_x$ is corroborated by another experiment where a 1 nm-thick Te layer is interposed between the Bi_2Te_3 and the Al film, and no Al delamination is observed (see Figure S2, Supporting Information). Nevertheless, the realization of $AlTe_x$ at the interface is detrimental due to its large bandgap and must be avoided.

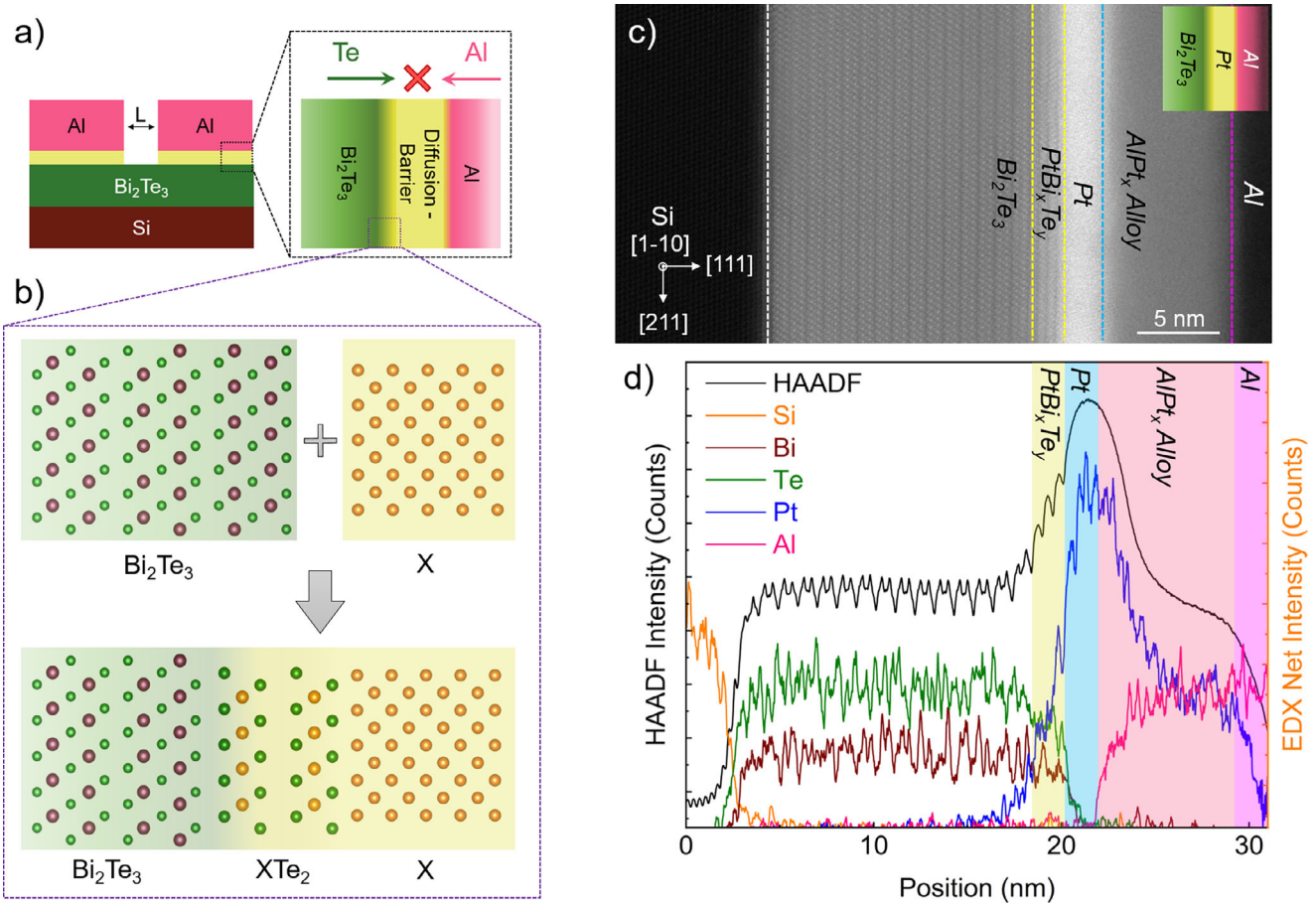

Figure 2. Incorporation of diffusion barrier and inhibition of Al diffusion: a) A schematic representation of Al-X-Bi_2Te_3-X-Al JJ, where X indicates an interlayer. A magnified region indicates that the main purpose of the interlayer is to block cross-diffusion of Al and Te to prevent the formation of $AlTe_x$. b) An atomic schematic illustrating the structural and chemical reconfiguration at the interface when an interlayer "X" transforms into its corresponding telluride "XTe_2" upon diffusion into the Bi_2Te_3 epilayer. c) A cross-sectional HAADF image of Si-Bi_2Te_3-Pt-Al heterostructure acquired along Si [1$\bar{1}$0] projection and the corresponding d) chemical profile confirming bidirectional diffusion of Pt into both Bi_2Te_3 and Al.

3. Diffusion Barrier and Impeding the Materialization of $AlTe_x$

The most viable and technically feasible option to prevent the diffusion of Al atoms into the Bi_2Te_3 epilayer is the incorporation of a diffusion barrier, that is, a thin interlayer at the interface. However, the material selection for an effective interlayer must be subject to strict criteria. The primary role of the interlayer, besides promoting adhesion, is to effectively impede the materialization of $AlTe_x$. In addition, the interlayer must be transparent to the Cooper pairs, which requires a metallic or semi-metallic composition. Additionally, it would be expedient if the interlayer could facilitate epitaxial integration with the Bi_2Te_3 epilayer. This would facilitate the mitigation of unwanted sources of noise at the interface due to structural incongruence causing strain and aberrations,[17] as well as chemical fluctuations due to compositional inhomogeneity.[38] The concept of interlayer incorporation at the interface is illustrated in **Figure 2a**. With all of the aforementioned requirements, the range of viable interlayers becomes fairly limited. This research focuses on four potential candidates: X = Nb, Ti, Pd, and Pt. A systematic, in-depth investigation is conducted to understand the advantages and disadvantages of each material and to scrutinize their usability in topological hybrid devices.

Several samples of Bi_2Te_3-X-Al heterostructures, with the above mentioned candidates, are prepared and no evidence of Al delamination is observed in any of those films. This confirms the enhanced adhesion of the interlayers to Bi_2Te_3 and Al and suggests possible structural and chemical reconfigurations at the interface due to a likely diffusion of interlayer atoms into the Bi_2Te_3 epilayer and/or Al. In view of this, the structural comprehension of the newly formed interfaces is of paramount importance prior to the superconducting transport investigation of JJs with interlayers (Al-X-Bi_2Te_3-X-Al).

Based on knowledge from previous reports,[39–41] investigations with Pt interlayers are initiated to determine the optimal deposition temperature and a suitable layer thickness. First, a Bi_2Te_3 epilayer is prepared on Si (111) substrate via MBE. Details of the growth parameters can be found here.[31] After the growth of Bi_2Te_3, the substrate is cooled to 150 °C where 5 nm of Pt is deposited in situ. STEM analysis revealed a highly deformed and amorphous interface with Pt atoms diffused deep into the TI epi-

layer. To improve the interface quality, Pt depositions are carried out at lower temperatures of 70 and 10 °C. Both temperatures resulted in improved, but not fully crystalline interfaces. A summary of temperature-dependent Pt deposition and the resulting interfaces can be found in Figure S3, Supporting Information. Nevertheless, the observation of exotic trilayer-like structures in several regions indicated structural reconfigurations with slightly improved crystal quality at 10 °C. It is worth mentioning that Pt is a transition metal which, upon interaction with Chalcogens (C = S, Se, Te, etc.), readily transforms into its corresponding chalcogenide, "PtC_2." Such alloys are commonly known as transition metal dichalcogenides (TMDCs), and most of them exhibit a trilayer-based trigonal crystal structure.[42] The presence of a trilayer structure at the interface of the probe prepared at 10 °C must be due to the formation of $PtTe_2$. For better understanding, this paradigm is illustrated in Figure 2b. Furthermore, a comprehensive chemical analysis of all the probes investigated revealed that the Pt interlayer with a reduced thickness of 3 nm would be sufficient to effectively inhibit the diffusion of Al atoms. Based on this, after Bi_2Te_3 epitaxy, the sample is cooled to −20 °C, and prior to Al metallization, a 3 nm-thick Pt layer is deposited, followed by extensive STEM and EDX analysis, as shown in Figure 2c,d, respectively.

An excellent crystal quality of Bi_2Te_3 with meticulously ordered quintuple layers and a pristine interface with Si (111) is evident in Figure 2c. A 1.5 nm-thick region with a Pt-based TMDC-like trilayer structure can be observed on top of Bi_2Te_3. This is followed by a 1.8 nm-thick layer of crystalline Pt (111). As mentioned above, lowering the deposition temperature regulates the diffusion of Pt into Bi_2Te_3, but not the diffusion into Al. The remaining Pt was found to be widely dispersed throughout the Al layer, up to a thickness of 7 nm, forming the $AlPt_x$ alloy. Unlike $AlTe_x$, $AlPt_x$ is not expected to form an electronic barrier at the interface due to its metallic properties. One approach to minimize the Pt diffusion into Al is to reduce the Pt thickness below 3 nm. A close examination of the EDX spectrum reveals that the Al and Te atoms are separated by only 1.5 nm. Reducing the Pt thickness can lead to crossover of Al and Te atoms, which can be catastrophic, as observed by the failure to achieve induced superconductivity in various junctions with Pt interlayers less than 3 nm-thick (see Figure S4, Supporting Information). After the $AlPt_x$ layer, a thick, crystalline Al film appears on top. Unlike Figure 1f, the crystal plane of Al cannot be observed here. This is due to a massive density mismatch between Pt and Al.

Using a similar mechanism, the optimal deposition temperatures for all interlayers are determined to be 50 °C for Nb and Ti and −20 °C for Pd and Pt. All interlayers are structurally and chemically characterized and demonstrated distinctive results; however, all interlayers have exhibited successful inhibition of $AlTe_x$ materialization at a thickness of 3 nm. Nb and Ti demonstrated the highest efficiency in inhibiting the diffusion of Al atoms, closely followed by Pt; while, Pd exhibited the lowest efficiency. A comparative analysis is shown in Figures S5–S7, Supporting Information.

4. Epitaxial Integration of XTe_2 with Bi_2Te_3

With improved adhesion and successful inhibition of $AlTe_x$ materialization, the primary objectives of the interlayers are achieved. However, with the diffusion of interlayer atoms into the TI epilayer, the enigma of achieving induced superconductivity now rests at the newly evolved interfaces between Bi_2Te_3 and the interlayers. This demonstrates the significance of Bi_2Te_3/X hybrid interfaces. The contemporary aim is to achieve electronically transparent, atomically sharp, defect-free, and epitaxial interfaces. Section 6 explores the interface transparency of each interlayer via superconducting transport of JJs. Meanwhile, this section focuses on understanding and manipulating the structural properties of newly evolved interfaces.

As mentioned earlier, the interlayers with cubic crystal structures, such as Nb, Pd, and Pt, are structurally incompatible with the trigonal Bi_2Te_3, which may hinder the formation of pristine interfaces. However, as shown in Figure 2c, Pt by diffusing into Bi_2Te_3 forms a $PtTe_2$-like structure. The materialization of this vdW-based trigonal structure leads to structural compatibility, allowing the formation of an epitaxial, atomically-uniform, fully-relaxed and incoherent interface with the Bi_2Te_3 surface. When the lattice sites of two crystals that do not exhibit a one-to-one correspondence, or when two materials with different in-plane lattices come into contact, an incoherent interface develops.[43,44] Incoherent interfaces between two incommensurate crystals exhibit no periodicity that leads to strain, whereas vdW interactions allow the realization of incoherent yet fully-relaxed and periodic interfaces.[43,44] This is a key feature of vdW interactions, since forcing the development of a coherent interface could lead to significant structural defects and strain.[30] Thus, the structural and electronic characteristics of the evolving interlayer-tellurides (XTe_2) and their incorporation onto the Bi_2Te_3 surface hold the key to functional devices.

4.1. Evolution of Interfaces in Nb and Ti interlayers

The Nb and Ti layers yielded completely unexpected results. In both cases there is no evidence of interlayer diffusion into the Bi_2Te_3 epilayer. However, the Bi_2Te_3 surface is still observed to restructure with the emergence of a distinct and epitaxially stacked bilayer. In the case of Nb, the emerging bilayer is followed by a trilayer-like structure and a 0.5 nm-thick somewhat amorphous layer, which precedes with the emergence of the Nb (220) crystal planes. **Figure 3a** depicts the scenario from top to bottom using STEM images, a diffraction intensity profile, and the corresponding EDX spectrum. The chemical analysis indicates the presence of a Bi-rich zone in the bilayer region, while the following 1 nm-thick region contains Nb and Te compositions. This is consistent with the hypothesis of $NbTe_2$ materialization, as observed in Figure 2 for Pt. Nevertheless, the formation of the bilayer and the subsequent structural aberrations are perplexing oddities that need to be elucidated.

Subsequent studies have shown that instead of diffusing into the Bi_2Te_3 epilayer, Nb atoms selectively consumed Te atoms at the epilayer surface to form $NbTe_2$. This process triggered the transformation of the topmost Bi_2Te_3 quintuple layer into a Bi_2 bilayer. A schematic demonstration is shown in Figure S8, Supporting Information. The newly formed $NbTe_2$ layer encountered two challenges: a scarcity of Te atoms and a significant (18.9%) lattice mismatch with the Bi_2 bilayer.[45] The emergence of the Bi_2 not only increased the lattice mismatch, but also led to the formation

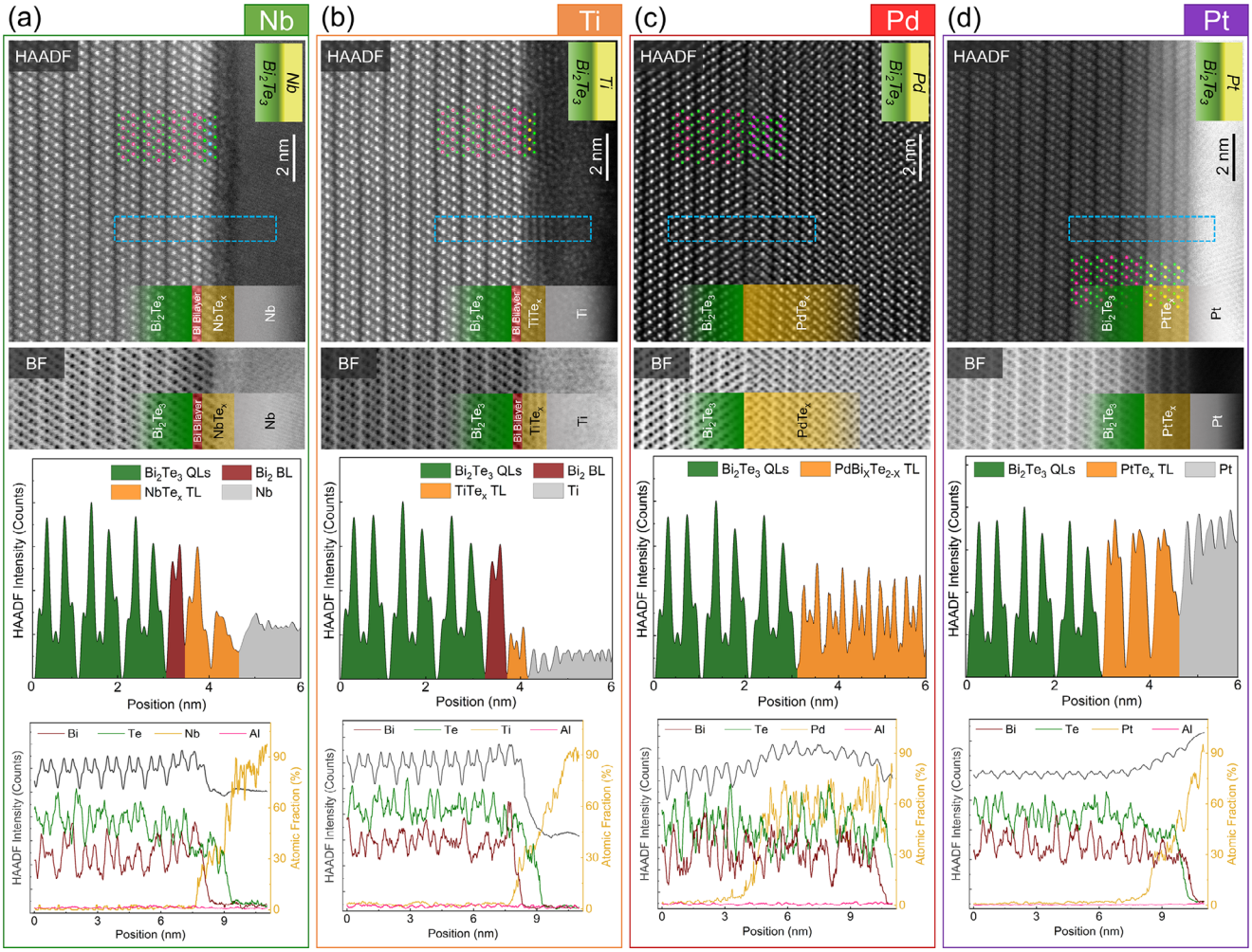

Figure 3. TMDCs assisted epitaxial integration of interlayers by transforming of interlayer "X" into its respective tellurides "XTe_2." From top to bottom: STEM-HAADF acquired along the Si [1$\bar{1}$0] projection, a bright field (BF) image of a selected region, the diffraction intensity profile of the highlighted region with yellow box and the EDX spectrum of Bi_2Te_3-X interfaces where X represents a) Nb, b) Ti, c) Pd, and d) Pt.

of hybrid/pseudo vdW gaps between Bi and Te atoms,[30] spanning between Bi_2Te_3/Bi_2 on one side and $Bi_2/NbTe_2$ on the other. The intricacies of the vdW bonding mechanism and its modifications are beyond the scope of this article. For details, please refer to our previous work.[30] Nevertheless, the vdW gap is observed to shrink at the Bi_2Te_3/Bi_2 interface due to the presence of relatively strong interactions between heterogeneous elements, namely Bi and Te (hybrid vdW). Due to these strong hybrid interactions, the Bi_2 bilayer forces the $NbTe_2$ layer to stretch laterally, forming a coherent interface. The Te deficiency, together with a substantial lateral strain, caused extensive damage to the $NbTe_2$ layer, resulting in the structural aberration depicted in Figure 3a. The Ti interlayer exhibited an analogous behavior to Nb. Figure 3b depicts the interface evolution in the Ti scenario.

It appears that the presence of a Bi_2 bilayer is the source of structural damage to $NbTe_2$ and $TiTe_2$. Since this is solely due to a Te deficiency at the Bi_2Te_3 surface, it can be mitigated by introducing excess Te. This will facilitate the development of a fully crystalline $Bi_2Te_3/NbTe_2$ and $Bi_2Te_3/TiTe_2$ interfaces. This hypothesis is confirmed by the co-evaporation of Ti and Te, which resulted in the formation of a fully relaxed, atomically sharp, epitaxial, and incoherent interface between Bi_2Te_3 and $TiTe_2$, as shown in Figures S9 and S10, Supporting Information. Similar experiments are performed with Nb and high-quality and relaxed heterostructures of Bi_2Te_3 and $NbTe_2$ are also obtained (Figure S9, Supporting Information). By manipulating the deposition parameters, it is possible to obtain both types of interfaces, with or without a Bi_2 bilayer, or in other words, coherent or incoherent interfaces, as desired. Although Nb and Ti exhibit structurally identical behavior, they are quite different electronically. $NbTe_2$ is a SC,[46] whereas a monolayer of $TiTe_2$ is a narrow bandgap semiconductor.[47] This difference could potentially affect the interface transparency in experiments involving superconducting transport. However, when $TiTe_2$ consists of two or more layers, it exhibits metallic behavior and should not be a concern,[47] since the thickness of $TiTe_2$ can be precisely controlled by co-evaporating Ti and Te atoms, as shown in Figure S10, Supporting Information.

4.2. Evolution of Interfaces in Pd interlayers

Pd, in contrast to Nb and Ti, exhibited significantly higher diffusion into the Bi_2Te_3 epilayer. By adjusting the deposition temperature to −20 °C, the diffusion of Pd was effectively confined to a depth of 9 nm. The Pd atoms diffused and bonded with nearby Te and Bi atoms, resulting in the formation of $PdBi_xTe_{2-x}$ trilayers. This inhibited the formation of Bi_2 bilayers, as observed for Nb and Ti interlayers. The STEM images and EDX analysis in Figure 3c illustrate the interface formation for the Pd interlayer. Detailed analysis revealed that the distribution of Pd atoms is not uniform throughout the diffused region. In close proximity to the Bi_2Te_3 surface, there is a relatively low concentration of Pd atoms, which transitioned into $PdTe_2$-like trilayers. These trilayers exhibited an epitaxial and well-defined interface with the Bi_2Te_3 epilayer. Away from the interface, the concentration of Pd atoms increased, leading to Pd intercalation at the vdW gaps. This process resulted in a non-layered, zig-zag structure that resembles PdTe. In short, the diffused zone consists of either Bi-doped $PdTe_2$ or $PdBi_xTe_{1-x}$, both of which exhibit superconductivity that attenuates as a function of Bi concentration, as demonstrated in our recent study.[48] As shown in Figure S7, Supporting Information, Pd permeates into Al, leading to the formation of the $AlPd_x$ alloy, which is also a superconducting alloy.[49] The Bi_2Te_3-Pd-Al heterostructure exhibits an intricate stack of multiple superconducting layers. Predicting the performance of such vertically stacked, atypical superconductors is almost impossible from a structural point of view. Only the superconducting transport analysis, discussed in Section 6, has the potential to provide a viable explanation.

4.3. Evolution of Interfaces in Pt interlayers

The diffusion of Pt into the Bi_2Te_3 epilayer and the subsequent formation of new regions has already been introduced in Figure 2. Pt demonstrated a diffusion pattern akin to Pd. Nevertheless, it exhibited a regulated behavior, where the diffusion length can be precisely controlled by the deposition conditions (see Figure S3, Supporting Information). The evolved interface for the Pt interlayer is shown in Figure 3d. By controlling the deposition parameters, the Pt diffusion is limited to a only 1.5 nm. A meticulous examination of this region has revealed the presence of three distinct trilayers composed of a $PtTe_2$-like structure. These trilayers exhibited epitaxial and atomically precise interfaces to both the Bi_2Te_3 and Pt (111) surfaces. In contrast to Pd, no intercalated atoms are observed at the vdW gaps. Furthermore, EDX analysis revealed a homogeneous distribution of Bi within the trilayers. This phenomenon can be attributed to an inherent tendency of Pt to form $PtTe_2$ and $PtBi_2$, which facilitates the formation of $PtBi_xTe_{2-x}$ trilayers.[30,50] The exact composition of the trilayer region is determined by EDX to be $PtBi_{0.7+x}Te_{1.3-x}$. Since both $PtTe_2$ and $PtBi_2$ are metallic, it is reasonable to assume that they would not pose a significant challenge to the induction of superconductivity.

Summarizing the Bi_2Te_3/X interfaces, all interlayers can be classified as non-diffusing, moderately diffusing, or strongly diffusing based on their interaction with the Bi_2Te_3 epilayer and the chemical analysis of the reconfigured surfaces. Nb and Ti are in the first category, Pt is in the second, and Pd is in the third. All interlayers allow the customization of the epitaxial interfaces through vdW stacking of TMDCs. Nb and Ti are the only options to design interfaces both with and without a Bi_2 bilayer. They also allow precise control of the number of TMDC layers by co-evaporation with Te. Pt and Pd, on the other hand, facilitate the diffusion-propagated synthesis of Bi-doped TMDCs, where the thickness can only be controlled by adjusting the deposition parameters. Pd, in particular, is an exception. Excessive diffusion into both Bi_2Te_3 and Al results in an enormously complex layer stack. Since $PdTe_2$ itself is a SC,[29] Pd integration with Al as the parent SC is the least suitable among all the interlayers. To gain further insight into the performance of each interlayer, ab initio modeling and superconducting transport analysis are employed and discussed in the subsequent sections.

5. Ab Initio Modelling of XTe_2/Bi_2Te_3 Interfaces

Motivated by the experimental observations discussed in the previous sections, a series of density functional theory (DFT) calculations are performed for the XTe_2/Bi_2Te_3 interface (see "Methods" Section for computational details). The four different XTe_2/Bi_2Te_3 (X = Nb, Ti, Pd, Pt) interfaces are compared, and the relaxed crystal structures for all four XTe_2/TI interfaces, both with and without an additional Bi_2 bilayer inserted at the interface to the TI, are computed. Comparable large formation energies of Bi_2 bilayers in all four XTe_2 interfaces are found. Thus, instead of being stabilized by a formation energy, it is speculated that the easy formation of PdBiTe and PtBiTe compounds in the cubic Ullmanite structure,[51,52] which do not exist for Nb and Ti-based compounds, might be an explanation for the absence of Bi_2 bilayers in the $PdTe_2$ and $PtTe_2$ heterostructures. However, the absence of the cubic Ullmanite structures in the experimental TEM data suggests a complicated influence of the surrounding matrix of trigonal TI and XTe_2 structures.

Regarding the influence on the electronic structure, it is found that the XTe_2 interface with Bi_2Te_3 generally leads to charge transfer between XTe_2 and the surface layers of the TI (see Figure S11, Supporting Information). The interfaces with X = Nb,Ti have the tendency to induce p-type doping to the TI, whereas this trend is less pronounced for X = Pd,Pt. This is seen in the position of the conduction band minimum and the location of the Dirac point of the TI's electronic structure, shown as the red-colored bands in **Figure 4**. The insertion of Bi_2 at the XTe_2/TI interface is furthermore acting as a charge donor, which results in n-type doping of the TI at the interface. Note that the simulations presented in Figure 4 are performed for intrinsically n-doped Bi_2Te_3, which reflects the experimental situation.

The states localized in the XTe_2 region of the computational unit cells are highlighted by the blue-colored bands in Figure 4. By comparing the four different XTe_2 interfaces, it can be seen that the band widths and details of the electronic structure of the TMDC are strongly influenced by the overlap of the wave function with the electronic structure of the TI. Moreover, the insertion of Bi_2 adds additional electronic states that hybridize in the calculated electronic structure (see also Figure S12, Supporting Information for region-projected electronic structure plots). We emphasize that in our DFT calculations all $XTe_2/[Bi_2]$ interfaces are metallic, supporting the conjecture from previous sections

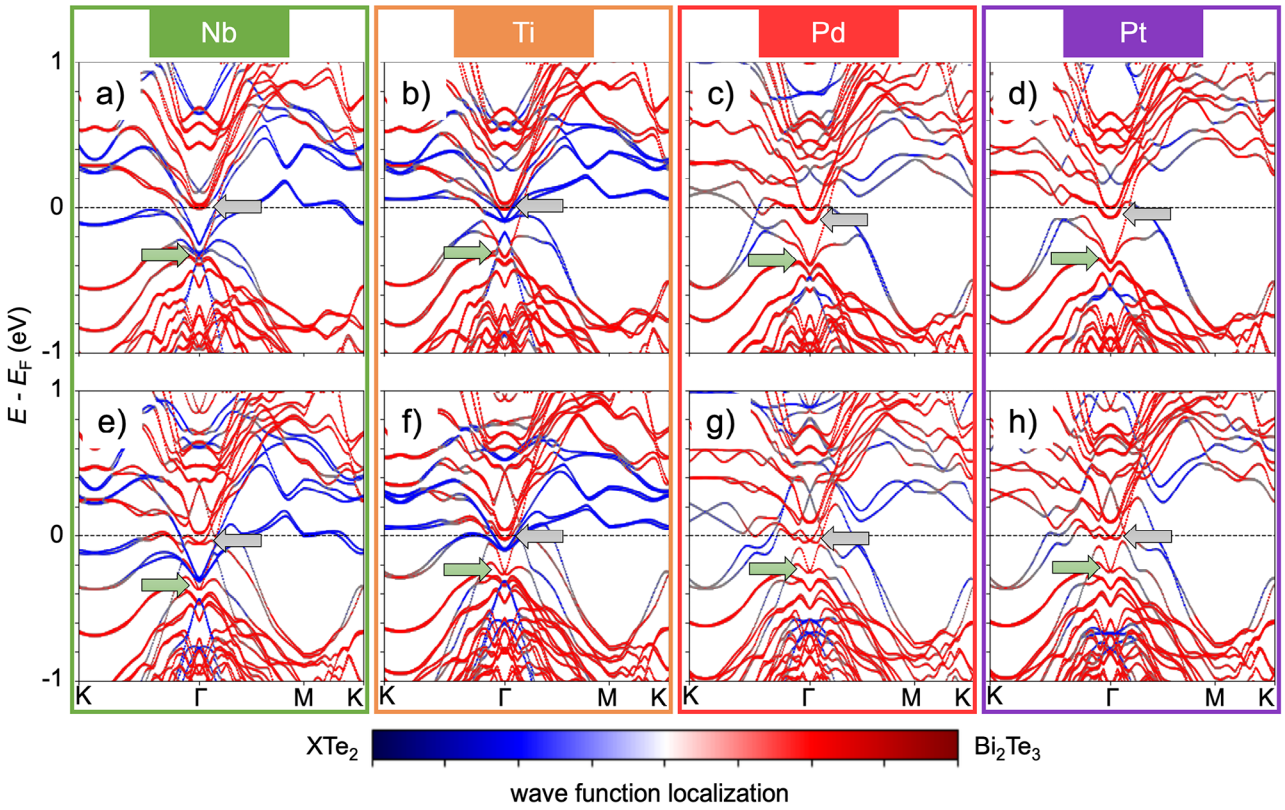

Figure 4. Normal state electronic structure of $XTe_2/[Bi_2]/(Bi_2Te_3)_3$. Structures without bismuth bilayer (Bi_2) for a–d) X = Nb, Ti, Pd, and Pt, respectively, and e–h) the same with Bi_2. Insertion of Bi_2 leads to a downward shift of the electronic structure seen in the location of the Dirac point and the conduction band minimum, highlighted by green and grey arrows, respectively. The coloring of the bands indicates the localization of the states where blue (red) states are localized in XTe_2/ (Bi_2Te_3). Note that an intrinsic *n*-type doping of the TI is assumed in the calculation.

that they can be proximitized from Al. Based on a comparison of the atom-projected band structures shown in Figure 4, clear pairwise similarities can be observed between X = Nb,Ti and X = Pd,Pt. We find a clear correlation with the differences in electronegativity of about 1.6 for Nb and Ti and 2.3 for Pd and Pt,[53] which is consistent with the classification into two distinct groups for X = Nb,Ti and X = Pd,Pt found in the structural analysis of Sections 3 and 4. This conjecture is further supported by the transport characterization discussed next.

6. Transport Characterization of Al-X-Bi_2Te_3-X-Al Josephson Junctions

To evaluate the performance of the different interlayers in TI-SC hybrid devices, we fabricated a sample with multiple Al-X-Bi_2Te_3-X-Al JJs for each interlayer using our UHV process (see "Methods" section for details). Thus, the Al-X-Bi_2Te_3 interfaces in the JJs should be comparable to the ones structurally investigated in the previous sections. Each sample contains several JJs with designed junction geometries ranging between $W = 300 - 1000$ nm and $L = 90 - 150$ nm. On the left in **Figure** 5a–d, an *IV* measurement is shown for one junction of each interlayer sample for both bias current sweep directions. In contrast to the increased resistance in junctions without an interlayer (see Figure 1), a finite supercurrent I_C is observed for the junctions with interlayers, indicating an improvement of the interfaces for all interlayers. A hysteresis between the switching current I_C and the retrapping current I_r, which is observed for the different sweep directions of some junctions (see Table S2, Supporting Information), is often attributed to heating effects in the resistive state for junctions in the given coplanar geometry.[54]

Using the critical current and the normal resistance R_n of the junctions, the I_CR_n product is calculated and compared to theoretical models. In Figure 5e, this I_CR_n product is shown for several JJs of each sample and plotted against their respective designed junction length. Following Cuevas et al.,[55] the grey shaded area in this figure indicates the expected I_CR_n values for an ideal junction in the diffusive transport regime with the typical range of parameters for the bulk-dominated Bi_2Te_3 films. For most of the Nb, Ti, and Pt interlayer junctions, the I_CR_n values are in this grey shaded region indicating that they fall in the range of ideal SNS junctions without additional interfacial barriers. A more detailed, quantitative analysis is, however, hampered by the range of material parameters for individual junctions (see supplementary Section 3–4). In contrast to these three interlayers, the I_CR_n values for the Pd interlayer junctions are significantly higher. While this is typically attributed to higher junction transparency, it should be treated with caution in this case. The I_CR_n data for these junctions exceed the expected diffusive transport regime and, in part, even an upper estimate for a short, ballistic junction (black dotted line in Figure 5e). Rather than a higher junction quality, we believe that this may be due to strong lateral

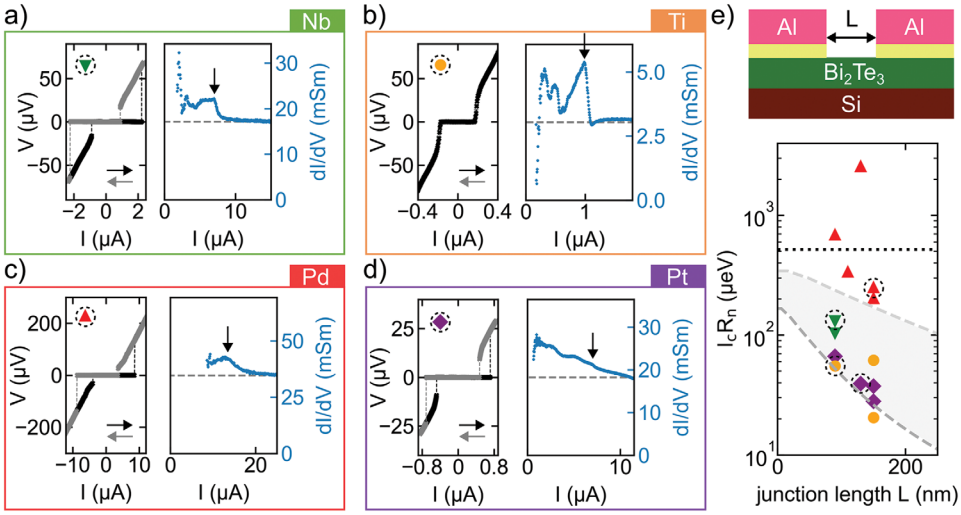

Figure 5. Electrical characterization of Al-X-Bi_2Te_3-X-Al JJs at cryogenic temperatures ($T < 50mK$), where X is a 3 nm interlayer of Nb (green), Ti (orange), Pd (red), or Pt (purple). a–d) *IV* characteristics for both sweep directions at a small range (left) and differential conductance at a larger range (right) for one junction of each respective interlayer sample. The grey dashed line in the right plot indicates the normal conductance $1/R_n$ of the junction and the black arrow indicates the outermost feature of the SGS. Graphs in (a) are adapted from Schmitt et al.[57] e) Top: Schematic of an Al-X-Bi_2Te_3-X-Al JJ with interlayer X = Nb, Ti, Pd, or Pt (yellow). Bottom: Extracted I_CR_n values for multiple JJs on each interlayer sample plotted against the designed junction length *L*. All junction parameters can be found in Table S2, Supporting Information. The encircled symbols mark the junctions shown in (a–d). The grey area indicates the theoretical length dependence of the I_CR_n values for an ideal junction in a diffusive transport regime with a superconducting coherence length of $\xi = 30 - 80nm$ and an induced gap of $\Delta^* = 80 - 165\mu eV$ according to Cuevas et al.[55] To estimate a general upper limit, the black dotted line indicates the limit of a ballistic junction with $\Delta^* = 165\mu eV$, which is the largest observed value for an induced gap in all characterized junctions (see Table S2, Supporting Information).

diffusion of Pd into the Bi_2Te_3 weak link, as reported by Rosen et al.[56] to be almost 40 nm in case of $(Bi,Sb)_2Te_3$, and the formation of a respective superconductive alloy. For junctions with long initial design geometries this could result in effectively shorter JJs (reduced L), whereas junctions with short initial design geometries might potentially be short-circuited (L → 0).

In addition to the *IV* measurement, the differential conductance dI/dV of each junction is plotted for a wider bias range on the right of Figure 5a–d. For all four junctions, the differential conductance shows an increased value of $dI/dV > 1/R_n$ at a bias current just exceeding I_C and continues to approach the normal conductance at larger bias (see supplementary Section 4 for a discussion of an even wider bias range). This observation of an increased conductance close to the superconducting state is typically attributed to the existence of multiple Andreev reflections in the junction. Such multiple Andreev reflections usually manifest in a sub harmonic gap structure (SGS) with features at $V = 2\Delta^*/ne$ in the differential conductance dI/dV, where *n* is an integer, *e* is the elementary charge, and Δ^* the induced gap. The exact nature of this SGS varies with respect to several parameters including the transport in the junction, the junction length, and the interface transparencies. So while the SGS features are assigned to conductance dips in transparent short ballistic JJs, they appear as peak-like structures in diffusive junctions with an intermediate length.[55,58] With respect to the bulk-dominated transport in the Bi_2Te_3 thin films, the JJs would fall in an intermediate long, diffusive junction regime (see supplementary Section 3–4). Accordingly, differential conductance peak features are observed in the measurements for all interlayer materials. With respect to the feature quantity and magnitude of the SGS, a variation is observed with more distinct features for the Ti and Nb interlayer junctions compared to the junction with Pd and Pt interlayer. This observation is, however, not unambiguously linked to the interlayer but could for example also be related to a different L/ξ range for the respective junctions, where ξ is the superconducting coherence length. For further analysis, we thus focus on the outermost feature of the SGS which is linked to $2\Delta^*/e$. This feature is indicated in the differential measurements of Figure 5a–d by a black arrow.

At the top of **Figure 6**a–d, the temperature dependence of the normalized differential conductance for the four JJs is plotted against the corresponding DC voltage *V*. In these measurements, the temperature-dependent position of the SGS features is traced to study the induced gap at the boundaries of the junction. For the Nb, Pd, and Pt interlayer junction, we observe an anomalous temperature-dependent change of the SGS features from peak-like features at low temperatures to dip-like features at higher ones. This anomalous transition is explained in more detail for the Nb junction in ref.[57] and could possibly be related to the existence of additional ballistic states superimposed on the diffusive bulk transport in the junction.

To study the induced gap Δ^* in this work, we extract the outermost peak-like feature at low temperatures as well as the dip-like feature at higher ones and skip the intermediate temperature range where neither can be assigned unambiguously. For the Ti interlayer, no anomalous transition is observed such that the position of the peak-like feature is extracted over the full temperature range of this junction. At the bottom of Figure 6a–d, the temperature-dependent feature position is shown and compared to the respectively scaled temperature dependence of a BCS gap

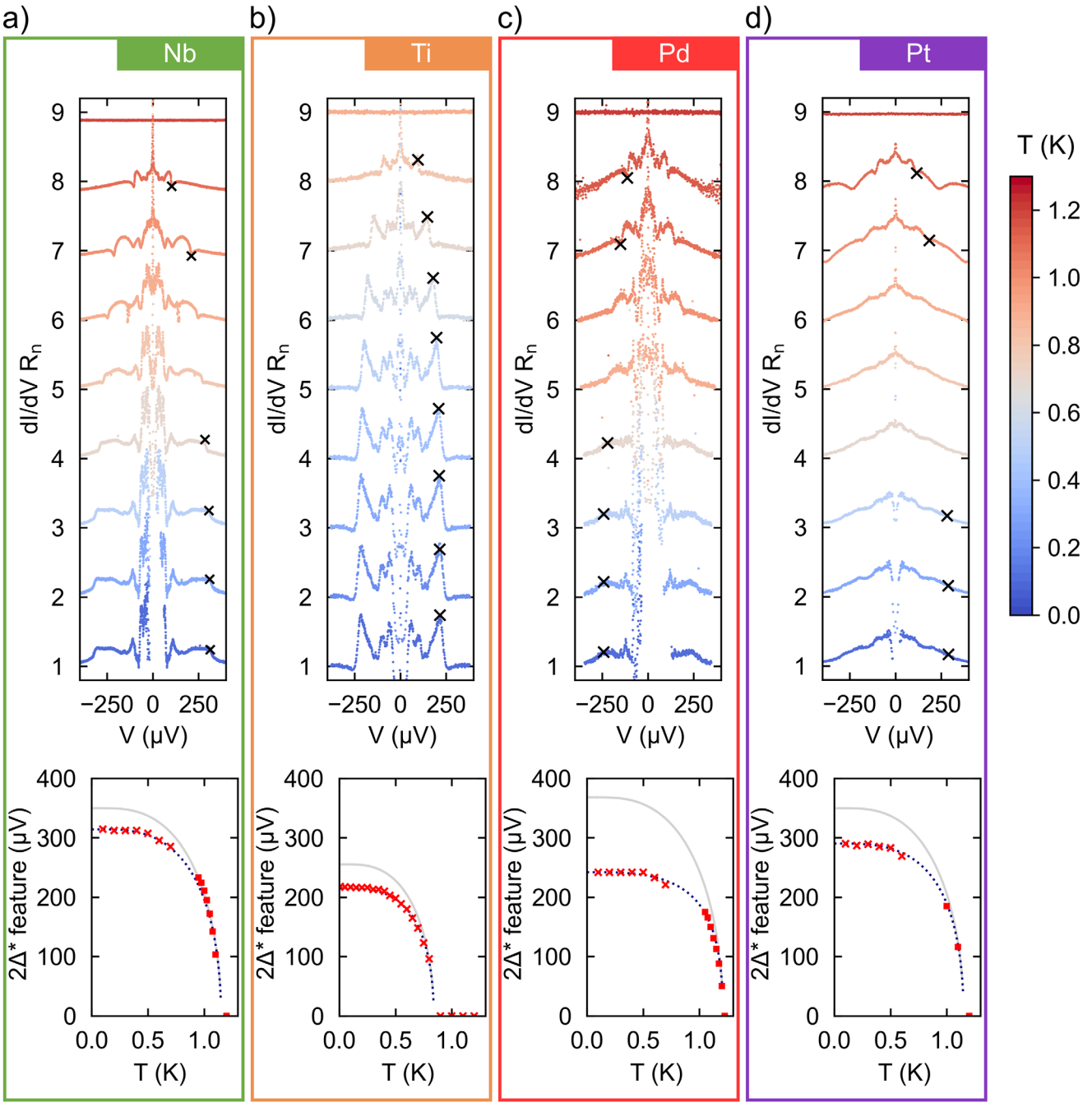

Figure 6. Temperature dependence of the differential conductance spectra for the JJs shown in Figure 5a–d. Top: Temperature dependence of the normalized differential conductance spectra plotted against the measured DC voltage V across the junction. For visibility the curves are shifted by 1. The black × indicates the position of the $2\Delta^*$ feature for curves where it could be assigned. Bottom: Temperature dependence of the assigned $2\Delta^*$ features with the peak-like features are indicated by a red × and dip-like features are indicated by a red box. The blue dotted line indicates the temperature dependence of an induced gap with the parameters listed in Table 1. The grey solid line shows the temperature dependence of a BCS gap with the same critical temperature. Graphs in Figure (a) are adapted from Schmitt et al.[57]

Δ_{BCS} (solid grey line) and an induced gap Δ^* (blue dotted line), where

$$\Delta^* = \frac{\Delta_{BCS}}{1 + \gamma_B \sqrt{\left(\Delta_{BCS}\right)^2 - \left(\Delta^*\right)^2}/\pi k_B T_C} \tag{1}$$

In this equation, T_C is the critical temperature, k_B is the Boltzmann constant, and γ_B parameterizes the interface transparency with $\gamma_B = 0$ for a perfectly transparent interface and $\gamma_B \to \infty$ for a vanishingly small interface transparency.[59] The values of the parameters γ_B and T_C for the plotted temperature dependence of Δ_{BCS} and Δ^* can be found in **Table 1**.

Table 1. Parameters of the induced gap temperature dependence for junctions shown in Figure 6. The critical temperature T_C and the interface parameter γ_B were used to fit the temperature dependence of an induced gap to the respective data. In addition, the ratio of the low temperature values for the induced gap (Δ_0^*) and a respective BCS gap with the same critical temperature ($\Delta_{BCS,0}$) are stated. For comparison, the last columns show the size of the gap (Δ_{DFT}) in the heterostructure relative to the size of the assumed pairing potential in XTe_2 ($\Delta_{DFT,0}$ = 3.07 meV) based on our KS-BdG calculations summarized in Figure 7.

Experiment				Theory	
Interlayer Material	T_C	γ_B	$\Delta_0^*/\Delta_{BCS,0}$	Unit Cell	$\Delta_{DFT}/\Delta_{DFT,0}$
Nb	1.15 K	0.45	0.90	$NbTe_2$ / Bi_2 / TI	0.98
Ti	0.84 K	0.55	0.85	$TiTe_2$ / Bi_2 / TI	0.80
Pd	1.21 K	1.20	0.66	$PdTe_2$ / TI	0.64
Pt	1.15 K	0.65	0.83	$PtTe_2$ / TI	0.85

While the critical temperature of the Nb, Pd, and Pt interlayer JJs fall in a similar range, it is significantly reduced for the Ti interlayer junction. To account for the individual critical temperature of each layer stack and thus facilitate the comparison of the respective induced gap, Table 1 also states the low temperature values of $\Delta_0^*/\Delta_{BCS,0}$. In general, the temperature dependence of an induced gap seems to describe the data well for all four interlayer junctions, however, it relies on a simple proximity interface model which does not allow to account for the details of the interfaces in the junctions under discussion. For this reason, DFT calculations for the proximity effect in the different layer stacks are discussed in the subsequent section.

7. First-Principles-Based Calculation of Superconducting Properties of XTe_2/TI Interfaces

To gain further insight into the relationship between the electronic structure and the proximity effect of the four different XTe_2/[Bi_2]/TI interfaces, we have performed DFT-based calculation for the superconducting state at these interfaces (see "Methods" Section for computational details).

Figure 7 shows the superconducting density of states (DOS) together with the superconducting order parameter χ. The DOS shown in Figure 7a,b is integrated over the entire unit cell, which manifests the fact that all states within the heterostructure will contribute to the transport through the JJs as the wavefunctions are typically delocalized over several layers across the interface. The DOS is suppressed around E_F due to the superconducting proximity effect in the heterostructure and the major coherence peaks are identified from the maximum of the anomalous DOS shown in Figure 7c,d. It is noteworthy that no complete suppression of the DOS at E_F is found due to details of the proximity effect in this complex heterostructure. In particular, some electronic states in XTe_2/TI only have a small wavefunction overlap with the states from the (by proximity to Al) superconducting XTe_2. This is, for instance, the case for the exponentially localized topological surface state at the TI/vacuum interface away from XTe_2. As a result, this strongly limits Cooper pair tunneling into these states and consequently no sizable superconducting gap is acquired.[60,61] Other states, on the other hand, have a larger wavefunction overlap with the electronic states of XTe_2 as seen from the normal state's bandstructures shown in Figure 4 where blue/red states overlap in different regions of the Brillouin zone.

Importantly, the electronic structure in these complex heterostructures is far from the idealized single-band BCS model and, thus, multi-band effects play an important role in the proximity effect.[62] Overall, the features of the superconducting DOS come out fairly similar for X = Nb, Ti, and Pt showing fairly sharp coherence peaks. However, for X = Pd the superconducting DOS and anomalous DOS appear broader and washed out. This leads to less sharp features which also results in a lower effective superconducting gap across the heterostructure. This can be deduced from the position of the major coherence peak in Figure 7. As in the normal-state properties, we find similarities between X = Nb,Ti on the one hand and X = Pd,Pt on the other hand, which we attribute to the formation of a Bi_2 bilayer in the former. The addition of Bi_2 acts as a further spacer layer in between the XTe_2 and the TI which reduces the size of the induced superconducting order parameter χ in the Bi_2Te_3 layers (see Figure S12, Supporting Information). Overall, χ decays rapidly away from the superconducting XTe_2. However, it is noteworthy that the size of the anomalous density is not necessarily the same as the size of the gap in the electronic structure.[63]

Table 1 compares the effective size of the gap in the calculations with the normalized experimental transport data ($\Delta_0^*/\Delta_{BCS,0}$). Overall, similar effective gap sizes are found with a maximal value in Nb and the smallest value in Pd due to the larger intermixing of the electronic structure. This correlates to the observed change in the interface transparency γ_B obtained from fitting the experimental transport data. However, it is important to note that, in contrast to the as-grown structures in the experiments, no chemical disorder is present in the DFT-based calculations of the superconducting state, which is particularly pronounced for the experimental Pd-based compounds, and which could be the driving force behind the different γ_B values found in the transport experiments. The fact that our DFT calculations, which only include the XTe_2-[Bi_2]-Bi_2Te_3 interface, agree well with the measured $2\Delta^*$ feature (Table 1), which are sensitive to the boundaries of the junction, suggest that the proximity effect through the Al-XTe_2-Bi_2Te_3 junction is not destroyed by the XTe_2 spacer layers. We suspect that the tendency of the studied XTe_2 interlayer compounds to become superconducting (see supplementary section 5) also plays a role for realizing functioning Al-X-Bi_2Te_3-X-Al Josephson junctions.[46,48,64,65]

A more quantitative comparison between theory and experiment would require not only including Al as a parent superconductor and thus much larger computational unit cells, but also a precise knowledge of the position of the Fermi level in the TI, and thicker XTe_2 as well as TI regions, which is computationally unfeasible. This could affect whether the XTe_2/TI interface leads to significant shifts in the Fermi level which, in turn, could induce band bending in the TI and the XTe_2 regions for large enough thicknesses.

8. Conclusion

In conclusion, this work paves the way for Al-based TI-SC hybrid devices by both tracing the absence of supercurrents in Al-

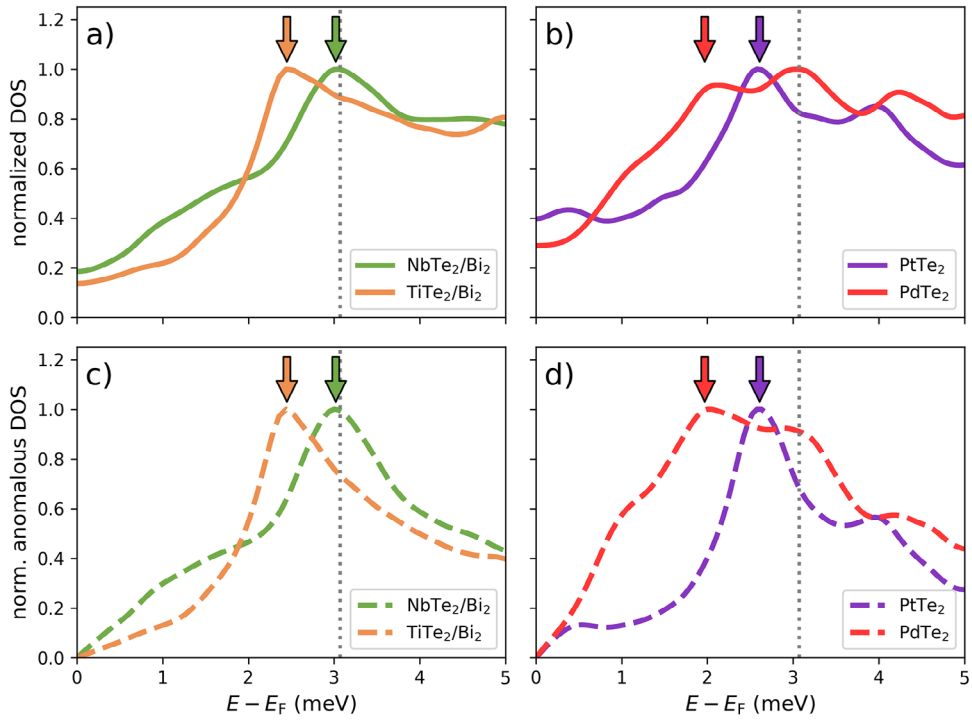

Figure 7. Calculated normalized superconducting (anomalous) density of states. a) DOS of $XTe_2/Bi_2/Bi_2Te_3$ (X = Nb,Ti) and b) of XTe_2/Bi_2Te_3 (X = Pt,Pd). c,d) Corresponding anomalous DOS (χ), which is the superconducting order parameter in the KS-BdG formalism. The colored arrows indicate the principal coherence peak identified by the maximum of χ in (c,d). The grey dotted line indicates the magnitude of the pairing potential in the XTe_2 region of the unit cell.

Bi_2Te_3-Al junctions to the detrimental materialization of $AlTe_x$, at the Bi_2Te_3-Al interface and investigating the improvement of this interface by the inclusion of four different thin interlayers (X), namely Nb, Ti, Pd, and Pt. Our study finds that these interlayers suppress the materialization of $AlTe_x$ at the Bi_2Te_3-X-Al interface while forming corresponding AlX alloys that enhance the adhesion of the Al layer. For the Bi_2Te_3-X interfaces, the diffusion and interaction of interlayers with Te atoms of the TI epilayer are found to promote the transformation into corresponding tellurides (XTe_2), leading to the formation of structurally compatible TMDCs. This process enables the tailoring of atomically-precise, relaxed, and vdW-based epitaxial interfaces with the Bi_2Te_3 epilayer. Through the characterization of UHV-fabricated Josephson junctions, the electrical improvement for the Bi_2Te_3-X-Al interfaces is revealed by finding supercurrents for all four investigated interlayers. While the parameters of junctions with Nb, Pt, and Ti interlayers reproducibly fall within the expected range for transparent Josephson junctions, the significant deviations found for junctions with Pd indicate that its use as an interlayer in devices might be hampered by the strong diffusion observed in the structural analysis. Our additional qualitative comparison for the induced superconductivity in different Bi_2Te_3-X-Al stacks, performed by both experimental observation of sub harmonic gap structures in JJs and complementary DFT-based calculations, can be used and extended for future research on Al-based hybrid devices to investigate them for, for example, parity-conserving transport. Our research not only establishes a foundation for advancing Bi_2Te_3-X-Al hybrid devices but also offers a flexible blueprint for inducing superconductivity in alternative topological materials, including $Bi_xSb_{2-x}Te_3$ alloys or Sb_2Te_3/Bi_2Te_3 heterostructures.[66] Furthermore, our findings extend to various parent superconductors, such as Pb and Sn, whose utilization is hindered by pronounced diffusion into the TI epilayers, too.[30] In sum this provides a comprehensive toolkit for precisely tailoring interfaces between superconducting and topological materials, enabling the evolution of the next generation of Majorana devices.

9. Experimental Section

Sample Fabrications: For the fabrication of Al-X-Bi_2Te_3-X-Al junctions both with and without an interlayer, an ultra-high vacuum fabrication process based on a stencil mask on Si (111) substrates was used. The details of mask fabrication can be found in the earlier report.[33] Subsequently, the sample was chemically cleaned and loaded into an MBE chamber and heated to 600 °C to ensure pristine 1×1 surface termination,[67] prior to selective area growth of 15 nm Bi_2Te_3 on the Si (111) surface under continuous sample rotation. Details of substrate cleaning and growth parameters can be found here.[30,31] Without breaking the vacuum, the sample was transferred to a second UHV chamber and cooled to −20 °C. For samples with interlayer, a layer of 3 nm Nb, Ti, Pd, or Pd was deposited without sample rotation and followed by the deposition of 40 nm Al. Then, a capping layer of 5 nm Al_2O_3 was deposited under continuous sample rotation and the sample is brought to ambient conditions. For the samples with interlayer, the excessive interlayer + Al stacks on the stencil mask (except in the very proximity of the junction) were finally removed by using standard photolithography techniques and wet chemical etching. For samples without an interlayer, this step was omitted due to adhesion problems.

TEM: For electron microscopy investigations, lamella specimens with dimensions of ≈4 µm × 10 µm were extracted at the cross-sections along the Si[1$\bar{1}$0] orientation using a focused ion beam (FIB, FEI Helios NanoLab 400S) system. A FEI Titan 80–200 ChemiSTEM microscope equipped with a HAADF detector and a Super-X spectrometer was used to collect the STEM image and EDX spectrum. With a semi-convergent angle at 24.7 mrad, the HAADF images were collected in an angular range of 70–200 mrad. The VESTA software package was used to draw the crystal structures. The lattice parameters of the XTe_2 and Bi_2Te_3 phases were measured and calibrated with respect to those of the Si substrate.

Transport: Electrical transport measurements on JJs were performed in a dilution refrigerator equipped with commercially available RF + RC filters and a base temperature of $T < 50$ mK. Each junction was measured in a current-biased quasi-four point measurement by applying a dc current I with an additional small low-frequency ac current for differential measurements. Both the dc voltage V and the differential resistance dV/dI were amplified at room temperature by differential amplifiers before being measured by a multimeter and a lock-in amplifier, respectively.

DFT Calculations: The DFT calculations relied on the full-potential linearized augmented planewave method as implemented in the $F_{LEUR\text{-}CODE}$ and the full-potential relativistic Korringa-Kohn-Rostoker Green function method (KKR) as implemented in the JuKKR code.[68–70] Superconducting properties were calculated with the help of the Kohn-Sham-Bogoliubov-de Gennes (KS-BdG) extension to the JuKKR code.[69] This work parametrized the normal state exchange correlation functional using the local density approximation (LDA) and added a constant superconducting pairing potential of *s*-wave symmetry within the XTe_2 atoms of the unit cell.[71] This work used an $l_{max} = 3$ cutoff in the angular momentum expansion of the space filling Voronoi cells around the atomic centers, where the exact (i.e., full-potential) description of the atomic shapes was taken into account.[72,73] Additional charge doping was added in a Lloyd's formula-like renormalization of the energy integration weights during self-consistency of the KKR calculations in this work.[74]

The structures that was studied computationally were interfaces between TMDC XTe_2 (X = Ti, Nb, Pt, Pd) and the prototypical TI Bi_2Te_3. The TI film that was used in the calculations for this work consist of three quintuple layer (QL) thick Bi_2Te_3 either directly in contact to a single TMDC trilayer or with an additional Bi_2 bilayer inserted in between. The unit cell was lattice matched to the in-plane unit cell of the TI and atomic positions at the interface were relaxed using the $F_{LEUR\text{-}CODE}$.[70] For this purpose this work set up symmetric films with 6 QL of the TI covered with an XTe_2 layer, optionally including a Bi_2 bilayer, and use the generalized gradient approximation with *van der Waals* corrections.[75,76] The relaxed interlayer distances are listed in Table S1, Supporting Information.

For the superconducting state this work then used the relaxed geometries from the normal state described in Section 5 and add a constant pairing potential in the solution to the Kohn-Sham Bogoliubov-de Gennes (KS-BdG) Hamiltonian,[69]

$$H^{KS}_{BdG}(x) = \begin{pmatrix} H^{KS}_0(x) - E_F & i\sigma_y \Delta_{DFT,0}(x) \\ -i\sigma_y \Delta_{DFT,0}(x) & -\left(H^{KS}_0(x) - E_F\right)^{\dagger} \end{pmatrix} \quad (2)$$

where $H^{KS}_0(x)$ is the normal states' Kohn-Sham Hamiltonian, E_F is the Fermi energy, x the position vector in the unit cell, σ_y is the Pauli matrix that ensures *s*-wave symmetry of the superconducting pairing, and $\Delta_{DFT,0}(x)$ denotes the spatially-dependent strength of the pairing potential. Here this work assumed $\Delta_{DFT,0}(x)$ to take a constant value of 3.07 meV within the XTe_2 layers and set $\Delta_{DFT,0} = 0$ everywhere else. This allowed studying the proximity effect within the four different $XTe_2/[Bi_2]/Bi_2Te_3$ heterostructures where in particular no intrinsic superconducting pairing is assumed within the TI layers. This approach was motivated from the experimental situation where thick Al serves as the parent superconducting compound that can proximitize the XTe_2 and subsequently the TI. While this model for the superconducting state was thus rather simple, taking into account the full orbital and multi-band description from DFT allowed making accurate predictions for the superconducting proximity effect.

Supporting Information

Supporting Information is available from the Wiley Online Library or from the author.

Acknowledgements

A.R.J. and T.W.S. contributed equally to this work. This work has been supported financially by the German Federal Ministry of Education and Research (BMBF) via Quantum Future project "MajoranaChips" (Grant No. 13N15264), the Bavarian Ministry of Economic Affairs, Regional Development and Energy for financial support within the High-Tech Agenda Project "Bausteine für das Quantencomputing auf Basis topologischer Materialien mit experimentellen und theoretischen Ansätzen" (Grant allocation No. 07 02/686 58/1/21 1/22 2/23) and the Deutsche Forschungsgemeinschaft (DFG, German Research Foundation) under Germany's Excellence Strategy – Cluster of Excellence Matter and Light for Quantum Computing (ML4Q) EXC 2004/1 – 39053469. The authors gratefully acknowledge the computing time granted through JARA on the supercomputer JURECA at Forschungszentrum Jülich (projects "superint" and "jiff13").

Open access funding enabled and organized by Projekt DEAL.

Conflict of Interest

The authors declare no conflict of interest.

Data Availability Statement

Raw data for experiments and calculations are openly accessible in a public data repository https://doi.org/10.24435/materialscloud:w3-3c. The FLEUR[70] and JuKKR[68] DFT codes are publicly available as open-source software under https://www.flapw.de and https://jukkr.fz-juelich.de.

Keywords

epitaxial interfaces, hybrid devices, interface engineering, josephson junctions, majorana platform, superconductors, TMDC, topological superconductivity

Received: July 20, 2024
Revised: September 25, 2024
Published online: November 5, 2024

[1] C. Nayak, S. H. Simon, A. Stern, M. Freedman, S. Das Sarma, *Rev. Mod. Phys.* **2008**, *80*, 1083.
[2] S. D. Sarma, M. Freedman, C. Nayak, *npj Quantum Inf.* **2015**, *1*, 15001.
[3] J. Alicea, *Rep. Prog. Phys.* **2012**, *75*, 076501.
[4] X. L. Qi, S. C. Zhang, *Rev. Mod. Phys.* **2011**, *83*, 1057.
[5] M. Sato, Y. Ando, *Rep. Prog. Phys.* **2017**, *80*, 076501.
[6] Y. Tanaka, S. Tamura, J. Cayao, *Prog. Theor. Exp. Phys.* **2024**.
[7] L. Fu, C. L. Kane, *Phys. Rev. Lett.* **2008**, *100*, 096407.
[8] C. W. J. Beenakker, *Annu. Rev. Condens. Matter Phys.* **2013**, *4*, 113.
[9] V. Mourik, K. Zuo, S. M. Frolov, S. R. Plissard, E. P. A. M. Bakkers, L. P. Kouwenhoven, *Science* **2012**, *336*, 1003.
[10] P. Krogstrup, N. L. B. Ziino, W. Chang, S. M. Albrecht, M. H. Madsen, E. Johnson, J. Nygård, C. M. Marcus, T. S. Jespersen, *Nat. Mater.* **2015**, *14*, 400.

[11] M. Sharma, P. Sharma, N. Karn, V. Awana, *Supercond. Sci. Technol.* **2022**, *35*, 083003.
[12] O. Breunig, Y. Ando, *Nat. Rev. Phys.* **2022**, *4*, 184.
[13] S. Kezilebieke, M. N. Huda, V. Vano, M. Aapro, S. C. Ganguli, O. J. Silveira, S. Glodzik, A. S. Foster, T. Ojanen, P. Liljeroth, *Nature* **2020**, *588*, 424.
[14] P. Zareapour, A. Hayat, S. Y. F. Zhao, M. Kreshchuk, A. Jain, D. C. Kwok, N. Lee, S.-W. Cheong, Z. Xu, A. Yang, G. D. Gu, S. Jia, R. J. Cava, K. S. Burch, *Nat. Commun.* **2012**, *3*, 1056.
[15] J.-P. Xu, M.-X. Wang, Z. L. Liu, J.-F. Ge, X. Yang, C. Liu, Z. A. Xu, D. Guan, C. L. Gao, D. Qian, Y. Liu, Q.-H. Wang, F. C. Zhang, Q. K. Xue, J.-F. Jia, *Phys. Rev. Lett.* **2015**, *114*, 017001.
[16] D. Kong, Y. Cui, *Nat. Chem.* **2011**, *3*, 845.
[17] N. P. de Leon, K. M. Itoh, D. Kim, K. K. Mehta, T. E. Northup, H. Paik, B. S. Palmer, N. Samarth, S. Sangtawesin, D. W. Steuerman, *Science* **2021**, *372*, eabb2823.
[18] F. Yang, Y. Ding, F. Qu, J. Shen, J. Chen, Z. Wei, Z. Ji, G. Liu, J. Fan, C. Yang, T. Xiang, L. Lu, *Phys. Rev. B* **2012**, *85*, 104508.
[19] M. Veldhorst, M. Snelder, M. Hoek, T. Gang, V. K. Guduru, X. L. Wang, U. Zeitler, W. G. van der Wiel, A. A. Golubov, H. Hilgenkamp, A. Brinkman, *Nat. Mater.* **2012**, *11*, 417.
[20] F. Qu, F. Yang, J. Shen, Y. Ding, J. Chen, Z. Ji, G. Liu, J. Fan, X. Jing, C. Yang, L. Lu, *Sci. Rep.* **2012**, *2*, 339.
[21] M. Bai, F. Yang, M. Luysberg, J. Feng, A. Bliesener, G. Lippertz, A. A. Taskin, J. Mayer, Y. Ando, *Phys. Rev. Mater.* **2020**, *4*, 094801.
[22] D. Zhang, J. Wang, A. M. DaSilva, J. S. Lee, H. R. Gutierrez, M. H. W. Chan, J. Jain, N. Samarth, *Phys. Rev. B* **2011**, *84*, 165120.
[23] J. R. Williams, A. J. Bestwick, P. Gallagher, S. S. Hong, Y. Cui, A. S. Bleich, J. G. Analytis, I. R. Fisher, D. Goldhaber-Gordon, *Phys. Rev. Lett.* **2012**, *109*, 056803.
[24] J. Shen, S. Heedt, F. Borsoi, B. van Heck, S. Gazibegovic, R. L. M. Op het Veld, D. Car, J. A. Logan, M. Pendharkar, S. J. J. Ramakers, G. Wang, D.i Xu, D. Bouman, A. Geresdi, C. J. Palmstrøm, E. P. A. M. Bakkers, L. P. Kouwenhoven, *Nat. Commun.* **2018**, *9*, 4801.
[25] I. Siddiqi, *Nat. Rev. Mater.* **2021**, *6*, 875.
[26] R. Barends, J. Kelly, A. Megrant, D. Sank, E. Jeffrey, Y. Chen, Y. Yin, B. Chiaro, J. Mutus, C. Neill, P. O'Malley, P. Roushan, J. Wenner, T. C. White, A. N. Cleland, J. M. Martinis, *Phys. Rev. Lett.* **2013**, *111*, 080502.
[27] W. Chang, S. M. Albrecht, T. S. Jespersen, F. Kuemmeth, P. Krogstrup, J. Nygård, C. M. Marcus, *Nat. Nanotechnol.* **2015**, *10*, 232.
[28] R. M. Lutchyn, E. P. A. M. Bakkers, L. P. Kouwenhoven, P. Krogstrup, C. M. Marcus, Y. Oreg, *Nat. Rev. Mater.* **2018**, *3*, 52.
[29] J. Zhang, C.-Z. Chang, Z. Zhang, J. Wen, X. Feng, K. Li, M. Liu, K. He, L. Wang, X. Chen, Q.-K. Xue, X. Ma, Y. Wang, *Nat. Commun.* **2011**, *2*, 574.
[30] A. R. Jalil, *Engineering Topological Superlattices and Their Epitaxial Integration in Selectively Grown Hybrid Nanostructures via MBE*, Halbleiter-Nanoelektronik, RWTH Aachen University, Germany **2022**.
[31] A. R. Jalil, P. Schüffelgen, H. Valencia, M. Schleenvoigt, C. Ringkamp, G. Mussler, M. Luysberg, J. Mayer, D. Grützmacher, *Nanomaterials* **2023**, *13*, 354.
[32] A. A. Volykhov, J. Sánchez-Barriga, A. P. Sirotina, V. S. Neudachina, A. S. Frolov, E. A. Gerber, E. Y.u. Kataev, B. Senkovsky, N. O. Khmelevsky, A. Y.u. Aksenenko, N. V. Korobova, A. Knop-Gericke, O. Rader, L. V. Yashina, *Chem. Mater.* **2016**, *28*, 8916.
[33] P. Schüffelgen, D. Rosenbach, C. Li, T. W. Schmitt, M. Schleenvoigt, A. R. Jalil, S. Schmitt, J. Kölzer, M. Wang, B. Bennemann, U. Parlak, L. Kibkalo, S. Trellenkamp, T. Grap, D. Meertens, M. Luysberg, G. Mussler, E. Berenschot, N. Tas, A. A. Golubov, A. Brinkman, T. Schäpers, D. Grützmacher, *Nat. Nanotechnol.* **2019**, *14*, 825.
[34] T. W. Schmitt, M. R. Connolly, M. Schleenvoigt, C. Liu, O. Kennedy, J. M. Chávez-Garcia, A. R. Jalil, B. Bennemann, S. Trellenkamp, F. Lentz, E. Neumann, T. Lindström, S. E. de Graaf, E. Berenschot, N. Tas, G. Mussler, K. D. Petersson, D. Grützmacher, P. Schüffelgen, *Nano Lett.* **2022**, *22*, 2595.
[35] P. Schüffelgen, D. Rosenbach, E. Neumann, M. P. Stehno, M. Lanius, J. Zhao, M. Wang, B. Sheehan, M. Schmidt, B.o Gao, A. Brinkman, G. Mussler, T. Schäpers, D. Grützmacher, *J. Cryst. Growth* **2017**, *477*, 183.
[36] J. Kölzer, A. R. Jalil, D. Rosenbach, L. Arndt, G. Mussler, P. Schüffelgen, D. Grützmacher, H. Lüth, T. Schäpers, *Nanomaterials* **2023**, *13*, 293.
[37] N. Prabhu, J. M. Howe, *Bull. Alloy Phase Diagrams* **1990**, *11*, 202.
[38] B. H. Elfeky, W. M. Strickland, J. Lee, J. T. Farmer, S. Shanto, A. Zarassi, D. Langone, M. G. Vavilov, E. M. Levenson-Falk, J. Shabani, *PRX Quantum* **2023**, *4*, 030339.
[39] S. Charpentier, L. Galletti, G. Kunakova, R. Arpaia, Y. Song, R. Baghdadi, S. M. Wang, A. Kalaboukhov, E. Olsson, F. Tafuri, D. Golubev, J. Linder, T. Bauch, F. Lombardi, *Nat. Commun.* **2017**, *8*, 2019.
[40] L. Galletti, S. Charpentier, Y. Song, D. Golubev, S. M. Wang, T. Bauch, F. Lombardi, *IEEE Trans. Appl. Supercond.* **2017**, *27*, 9900445.
[41] G. Kunakova, T. Bauch, E. Trabaldo, J. Andzane, D. Erts, F. Lombardi, *Appl. Phys. Lett.* **2019**, *115*, 172601.
[42] S. Manzeli, D. Ovchinnikov, D. Pasquier, O. V. Yazyev, A. Kis, *Nat. Rev. Mater.* **2017**, *2*, 17033.
[43] A. E. Romanov, T. Wagner, M. Rühle, *Scr. Mater.* **1998**, *38*, 869.
[44] R. Dingreville, A. Hallil, S. Berbenni, *J. Mech. Phys. Solids* **2014**, *72*, 40.
[45] B. E. Brown, *Acta Crystallogr.* **1966**, *20*, 264.
[46] S. Nagata, T. Abe, S. Ebisu, Y. Ishihara, K. Tsutsumi, *J. Phys. Chem. Solids* **1993**, *54*, 895.
[47] D. K. G. de Boer, C. F. van Bruggen, G. W. Bus, R. Coehoorn, C. Haas, G. A. Sawatzky, H. W. Myron, D. Norman, H. Padmore, *Phys. Rev. B* **1984**, *29*, 6797.
[48] X.-K. Wei, A. R. Jalil, P. Rurmann, Y. Ando, D. Grutzmacher, S. Blugel, J. Mayer, *ACS Nano* **2023**, *18*, 571.
[49] C. Friedberg, A. Rex, J. Ruvalds, *Phys. Rev. B* **1979**, *19*, 5694.
[50] Y.a Feng, Q.i Jiang, B. Feng, M. Yang, T. Xu, W. Liu, X. Yang, M. Arita, E. F. Schwier, K. Shimada, H. O. Jeschke, R. Thomale, Y. Shi, X. Wu, S. Xiao, S. Qiao, S. He, *Nat. Commun.* **2019**, *10*, 4765.
[51] F. Hulliger, *Nature* **1963**, *198*, 382.
[52] J. D. Childs, S. R. Hall, *The Canadian Mineralogist* **1973**, *12*, 61.
[53] D. R. Lide, *CRC Handbook of Chemistry and Physics*, CRC Press, Boca Raton **2004**.
[54] H. Courtois, M. Meschke, J. Peltonen, J. P. Pekola, *Phys. Rev. Lett.* **2008**, *101*, 067002.
[55] J. C. Cuevas, J. Hammer, J. Kopu, J. K. Viljas, M. Eschrig, *Phys. Rev. B* **2006**, *73*, 184505.
[56] I. T. Rosen, C. J. Trimble, M. P. Andersen, E. Mikheev, Y. Li, Y. Liu, L. Tai, P. Zhang, K. L. Wang, Y.i Cui, M. A. Kastner, J. R. Williams, D. Goldhaber-Gordon, *Phys. Rev. B* **2024**, *110*, 064511.
[57] T. W. Schmitt, B. Frohn, W. Wittl, A. R. Jalil, M. Schleenvoigt, E. Zimmermann, A. Schmidt, T. Schapers, J. C. Cuevas, A. Brinkman, D. Grutzmacher, P. Schuffelgen, *Supercond. Sci. Technol.* **2023**, *36*, 024002.
[58] D. Averin, A. Bardas, *Phys. Rev. Lett.* **1995**, *75*, 1831.
[59] B. A. Aminov, A. A. Golubov, M. Y. Kupriyanov, *Phys. Rev. B* **1996**, *53*, 365.
[60] G. Csire, B. Újfalussy, J. Cserti, B. Győrffy, *Phys. Rev. B* **2015**, *91*, 165142.
[61] K. Park, G. Csire, B. Ujfalussy, *Phys. Rev. B* **2020**, *102*, 134504.
[62] P. Rüßmann, M. Bahari, S. Blügel, B. Trauzettel, *Phys. Rev. Res.* **2023**, *5*, 043181.
[63] C.-K. Chiu, W. S. Cole, S. Das Sarma, *Phys. Rev. B* **2016**, *94*, 125304.
[64] D. Wu, Y. Lin, L. Xiong, J. Li, T. Luo, D. Chen, F. Zheng, *Phys. Rev. B* **2021**, *103*, 224502.

[65] U. Dutta, P. S. Malavi, S. Sahoo, B. Joseph, S. Karmakar, *Phys. Rev. B* **2018**, *97*, 060503.
[66] M. Eschbach, E. Mlynczak, J. Kellner, J. Kampmeier, M. Lanius, E. Neumann, C. Weyrich, M. Gehlmann, P. Gospodaric, S. Döring, G. Mussler, N. Demarina, M. Luysberg, G. Bihlmayer, T. Schäpers, L. Plucinski, S. Blügel, M. Morgenstern, C. M. Schneider, D. Grützmacher, *Nat. Commun.* **2015**, *6*, 8816.
[67] A. R. Jalil, X. Hou, P. Schüffelgen, J. H. Bae, E. Neumann, G. Mussler, L. Plucinski, D. Grützmacher, *Nanomaterials* **2023**, *13*, 2143.
[68] P. Rüßmann, D. Antognini Silva, D. S. G. Bauer, P. Baumeister, P. F. Bornemann, J. Bouaziz, S. Brinker, J. Chico, P. H. Dederichs, B. H. Drittler, F. Dos Santos, M. dos Santos Dias, N. Essing, G. Géranton, I. Klepetsanis, A. Kosma, N. H. Long, S. Lounis, P. Mavropoulos, E. Mendive Tapia, C. Oran, N. Papanikolaou, E. Rabel, B. Schweflinghaus, N. Stefanou, A. R. Thiess, R. Zeller, B. Zimmermann, S. Blügel, FLEUR, **2022**.
[69] P. Rüßmann, S. Blügel, *Phys. Rev. B* **2022**, *105*, 125143.
[70] D. Wortmann, G. Michalicek, N. Baadji, W. Beida, M. Betzinger, G. Bihlmayer, T. Bornhake, J. Bröder, T. Burnus, J. Enkovaara, F. Freimuth, C. Friedrich, C.-R. Gerhorst, S. Granberg Cauchi, U. Grytsiuk, A. Hanke, J.-P. Hanke, M. Heide, S. Heinze, R. Hilgers, H. Janssen, D. A. Klüppelberg, R. Kovacik, P. Kurz, M. Lezaic, G. K. H. Madsen, Y. Mokrousov, A. Neukirchen, M. Redies, S. Rost, et al., FLEUR, **2023**.
[71] S. H. Vosko, L. Wilk, M. Nusair, *Can. J. Phys.* **1980**, *58*, 1200.
[72] N. Stefanou, H. Akai, R. Zeller, *Comput. Phys. Commun.* **1990**, *60*, 231.
[73] N. Stefanou, R. Zeller, *J. Phys.: Condens. Matter* **1991**, *3*, 7599.
[74] Z. Rudolf, *J. Phys.: Condens. Matter* **2004**, *16*, 6453.
[75] J. P. Perdew, K. Burke, M. Ernzerhof, *Phys. Rev. Lett.* **1996**, *78*, 1396.
[76] S. Grimme, J. Antony, S. Ehrlich, H. Krieg, *J. Chem. Phys.* **2010**, *132*, 154104.